Dynamic Modeling and Analysis of a Driving Passenger Vehicle

Seen Yun , Jeonga Lee , Woojae Jang , Daeji Kim , Minseok Choi , Jintai Chung *

Posted Date: 19 April 2023

doi: 10.20944/preprints202304.0529.v1

Keywords: dynamic analysis; dynamic model; dynamic responses; mode shapes; natural frequencies; suspension deformations; vehicle driving test; steering conditions

Article

Dynamic Modeling and Analysis of a Driving Passenger Vehicle

Seen Yun [1], Jeonga Lee [1], Woojae Jang [1,4], Daeji Kim [1,3], Minseok Choi [2] and Jintai Chung [1,4,*]

[1] Department of Mechanical Engineering, Hanyang University, Ansan 15588, Republic of Korea; syyn1@hanyang.ac.kr (S.Y.); dlzh93@hanyang.ac.kr (J.L.); woojae123@hanyang.ac.kr (W.J.); hidada1004@hanyang.ac.kr (D.K.)
[2] Hyundai Motor Company, Hwaseong 18280, Republic of Korea; ms.choi@hyundai.com (M.C.)
[3] Korea Institute of Industrial Technology, Daegu 42990, Republic of Korea
[4] BK21 FOUR ERICA-ACE Center, Hanyang University, Ansan 15588, Republic of Korea; BK21 FOUR ERICA-ACE Center, Hanyang University, Ansan 15588, Republic of Korea
* Correspondence: jchung@hanyang.ac.kr

Abstract: This study presents a dynamic model of a passenger vehicle and analyzes its dynamic characteristics and responses. A dynamic vehicle model with seven degrees of freedom was established to analyze the behavior of a driving vehicle. The vehicle model had three degrees of freedom for the motion of the sprung mass and four degrees of freedom for the unsprung masses. For this model, the equations of motion were derived using Lagrange's equation. To verify the model, the suspension deformations computed using the model were compared with the deformations measured through three actual vehicle driving tests which are the slalom, double lane change, and step steer tests. Furthermore, we investigated the effects of suspension stiffness, suspension damping, and anti-roll bar torsional stiffness on the dynamic characteristics and responses of the vehicle model. The developed dynamic vehicle model may help vehicle designers predict the dynamic responses of a vehicle through simulation without performing a driving test.

Keywords: dynamic analysis; dynamic model; dynamic responses; mode shapes; natural frequencies; suspension deformations; vehicle driving test; steering conditions

1. Introduction

The ride comfort of vehicles has continuously improved in response to the diverse needs of consumers over the years. Previously, with degraded road environments, ride comfort was evaluated according to the behavior of a vehicle traveling on an uneven road surface. However, in recent years, when the road environment has improved, the behavior of the vehicle based on the steering wheel operation of driver on a uniform road surface also has a significant influence on the evaluation of riding comfort. To satisfy the riding comfort performance with the conditions mentioned above and consumers demand, automobile manufacturers have continuously conducted driving tests using numerous test vehicles from the past and have evaluated and improved ride comfort through the analysis of driving test results. However, the driving test process is time consuming and expensive that involves the vehicle design stage, developing a prototype, and preparing and performing the test. In addition, variables such as external environmental factors during the driving test and the driver's driving condition may adversely affect the reliability of the test. Therefore, to address the shortcomings and limitations of these driving tests, various studies are being conducted to establish a vehicle dynamics model and evaluate and improve riding comfort through simulations.

Based on the procedures of various driving tests, studies have been conducted to analyze ride comfort through the simulation of vehicle models. Accordingly, some notable studies related to driving tests are summarized. Choi et al. [1] experimentally measured and evaluated the vertical direction (bounce) and front-rear tilting (pitch) behavior of a vehicle body, which occurs predominantly when the vehicle passes through an uneven road surface during the test. Jonsson and Johansson designed a suspension system that can control bounce and pitch behavior to improve

riding comfort [2]. On the other hand, the left and right tilting (roll) behavior of the vehicle body while turning on a flat road surface is also very important considering the ride comfort and stability. In this regard, Uys et al. [3] experimentally evaluated the roll behavior caused by changing the steering wheel of a driving vehicle, and Darling and Hickson [4] developed an anti-roll suspension system that can improve riding comfort by controlling roll behavior. Further, Choi et al. [5] performed an experiment suggesting a method to control the damping characteristics of the suspension to improve riding comfort by considering the body bounce, pitch, and roll behaviors that were separately considered in previous studies.

Studies on the analysis of ride comfort through simulation after expressing vehicle systems as simple dynamic models have been published; and they are mainly based on the quarter-car model considering only the vertical behavior of the vehicle body. Sun et al. [6] established a two-degree-of-freedom vehicle model with vertical road surface excitation and derived the equation of motion using the Lagrange equation. Subsequently, the vertical vibration of the vehicle body according to the change in parameters such as mass, stiffness, and damping ratio in the model was analyzed through numerical analysis. Georgiou et al. [7] presented an optimization technique for deriving optimum values of damping and stiffness of suspension for improved ride comfort with vehicle models, including manual and semi-active suspension. Singh et al. [8,9] established a model by additionally considering a seat and a human body in a quarter-car model that depicts only existing vehicles and suggested a method to improve ride comfort through vibration responses from seats or body parts according to vertical road excitation.

After that, the vehicle model was expanded from the existing quarter-car model to the half-car model to consider the tilting behavior of the car body. Some studies that analyzed ride comfort using this model are as follows. Sun et al. [10] derived the equations of motion for a vehicle model with four degrees of freedom that can consider the bounce and pitch of the vehicle body traveling on a rough road. They analyzed various responses in the time and frequency domains for the change of model parameters. Zhu et al. [11] obtained frequency response functions for random road excitation through a vehicle model considering the pneumatically interconnected suspension (PIS) system and compared and analyzed them with the vehicle model without the PIS system. On the other hand, Hudha et al. [12], who were interested in the roll behavior of the vehicle body, established a vehicle model with the effect of the anti-roll bar and the control arm, and presented a suspension control system that can control the roll of the vehicle body caused by road excitation. Gosselin-Brisson et al. [13] proposed an active anti-roll bar system that can effectively control the roll motion of the vehicle body caused by lateral acceleration under vehicle turning conditions.

Recent studies analyzed the riding comfort with a full car model to better realize the behavior of the actual vehicle. Abu Bakar et al. [14] proposed a full car model with seven degrees of freedom that can analyze ride comfort. To verify the proposed model validity, the similarity between the simulation and experimental results was shown in the pitch mode test condition of the vehicle body that occurs when passing through a bump. Palli et al. [15] and Sentilkumar et al. [16] established a full vehicle model with seven degrees of freedom considering active suspension and found that active suspension improves riding comfort by preventing vehicle resonance that may occur due to road excitation. On the other hand, Ghike and Shim [17] proposed a full car model with 14 degrees of freedom that can analyze the rolling behavior of a turning vehicle according to steering conditions. He also showed the limitations of his model and demonstrated its excellence and validity.

With improvement in road environment along with recent developments in the vehicle industry, vehicle consumers are demanding improvements in ride comfort performance according to the driver's steering conditions, and not just the ride comfort performance against irregular road surface disturbances. In this regard, various vehicle manufacturers have attempted to analyze and improve ride comfort through driving tests; however, a time-efficient and affordable method is needed for driving tests to quickly respond to consumer demands. Therefore, building a simple mathematical model of a vehicle that can analyze the riding comfort of a vehicle driven by steering input through simulation is desired.

 doi:10.20944/preprints202304.0529.v1

However, most of the existing studies investigated by the author tend to focus on vehicle models for analyzing ride comfort under disturbance conditions, such as uneven road surfaces or irregularities. In addition, several studies have been published to analyze the behavior of the vehicle body by establishing a vehicle model for turning conditions; however, they have used a method to obtain a response generated by inputting an arbitrary lateral acceleration to the vehicle body. However, because lateral acceleration is a variable determined by the change in the steering angle input by the driver, it is limited as an actual input condition for a turning vehicle. Therefore, in this study, a full-car model that can analyze the riding comfort of a turning vehicle according to the change in steering angle, which is the driver's input condition, was presented. The new 7-DOF full car model proposed in this study is valuable in that the simulation and driving test results for various steering conditions have been comparatively verified.

The remainder of this paper is organized as follows. In Section 2, a dynamic vehicle model that can analyze the behavior of a driving passenger car is developed. A vehicle model with seven degrees of freedom was established, considering the centrifugal force acting on the vehicle during turning and the torsional stiffness of the anti-roll bar. Based on this model, the equations of motion are derived using Lagrange's equation. In Section 3, the established vehicle model is verified by comparing the vertical suspension deformations computed with the vehicle model with the deformations measured through actual vehicle driving tests. For comparison, three driving tests were performed: the slalom, double lane change, and step steer tests. In Section 4, the natural frequencies and mode shapes of the dynamic vehicle model are computed and analyzed using the developed vehicle model. Furthermore, the effects of changes in the design parameters on the dynamic response of the vehicle model were investigated. The considered design parameters were the suspension stiffness, suspension damping, and anti-roll bar torsional stiffness. Finally, conclusions and a summary of the study results are presented in Section 5.

2. Dynamic Vehicle Model

In this section, a dynamic model of a vehicle that can analyze the behavior of a driving passenger car is presented. This study assumes that the speed of the vehicle is kept constant, and the driving direction of the vehicle is changed by the steering wheel. Under these assumptions, the vehicle does not accelerate in the longitudinal direction (direction of travel), but only accelerates in the lateral direction perpendicular to the traveling direction. This lateral acceleration imparts a centripetal force to the vehicle and maintains it on a turning trajectory. A centrifugal force equal in magnitude to this centripetal force, but opposite in direction, acts on the vehicle to generate movement of the vehicle body. Therefore, to establish a dynamic vehicle model for analyzing the behavior of a turning vehicle, the centrifugal force generated by the turning of the vehicle must be considered.

The centrifugal force acting on the vehicle during turning is given by the following equation:

$$F = m_t \frac{V^2}{R} \tag{1}$$

where m_t is the total mass of the vehicle, V is the speed of the vehicle, and R is the turning radius. As the mass m_t and speed V are constant when the vehicle is traveling at a constant speed, the centrifugal force F is determined by the turning radius R.

The relationship between the turning radius of the vehicle and steering angle of the steering wheel was analyzed. First, the relationship between the vehicle's turning radius and steering angles of the front wheels can be derived from the Ackermann steering geometry [18], as shown in Figure 1. In Figure 1, point O is the instantaneous turning center, G is the center of mass of the vehicle, l_1 and l_2 are the distances from the center of mass to the front and rear wheels, respectively, w is the distance between the centers of the left and right wheels, and L is the distance from the front wheel to the rear wheel. As shown in this figure, the position of the turning center O coincides with the intersection of the extension line of the rear axle and the vertical lines inside and outside the front wheels. Accordingly, the steering angle of the inner front wheel δ_i is formed by the extension line of the rear axle and a line perpendicular to the inner front wheel, and the steering angle of the outer

Preprints (www.preprints.org) | NOT PEER-REVIEWED | Posted: 19 April 2023 doi:10.20944/preprints202304.0529.v1

wheel δ_o is formed by the extension line and a line perpendicular to the outer front wheel. The distance R from the turning center O to the vehicle center of mass G is called the turning radius, and the distance from the turning center O to the center of the rear axle is expressed as R_r.

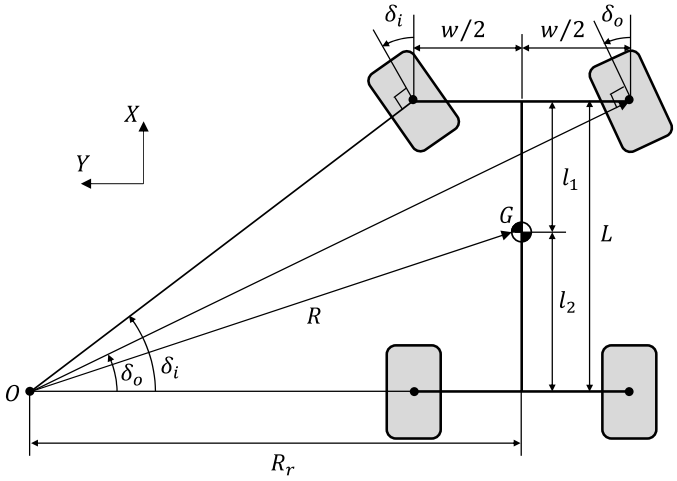

Figure 1. Ackermann steering geometry for the front steer angles of the inner and outer wheels.

Thus, if the instantaneous turning center is determined geometrically, the turning radius R can be expressed as the inner and outer front wheel steering angles δ_i and δ_o. The relationship between the steering angles of the inner and outer front wheels, the distance from the turning center to the center of the rear wheel axle, and the distance between the left and right wheels can be expressed by the following equations.

$$\tan \delta_i = \frac{L}{R_r - w/2} \tag{2}$$

$$\tan \delta_o = \frac{L}{R_r + w/2} \tag{3}$$

In general, as the steering angle is not large when the vehicle is traveling, the steering angles δ_i and δ_o are assumed to be small, and the turning radius R is very large compared to the distance w between the centers of the left and right wheels. Therefore, in Equations (2) and (3), $\tan \delta_i$ and $\tan \delta_o$ can be approximated by δ_i and δ_o, the distance from the turning center to the center of the rear wheel axle R_r can be replaced by the turning radius R, and the distance between the left and right wheels w can be neglected. Denoting the average steering angles of the inner and outer front wheels by δ, that is, $\delta = (\delta_i + \delta_o)/2$, the turning radius of the vehicle is given by:

$$R = \frac{L}{\delta} \tag{4}$$

This equation implies that the turning radius R is determined by the average steering angle of the front wheels δ and wheelbase distance L.

The centrifugal force applied to a turning vehicle can be obtained by substituting Equation (4) into Equation (1).

$$F = \frac{m_t V^2 \delta}{L} \tag{5}$$

The average steering angle of the front wheels is determined by the steering ratio and steering wheel angle, which can be expressed by the following equation [19]:

$$\delta_s = i_s \delta \tag{6}$$

where δ_s is the angle of the steering wheel and i_s is the steering ratio of the steering wheel angle to the steering angle of the front wheels. The steering angle ratio i_s is determined by the gear ratio of

Preprints (www.preprints.org) | NOT PEER-REVIEWED | Posted: 19 April 2023 doi:10.20944/preprints202304.0529.v1

the steering linkage connecting the steering wheel and the front wheel, and 15 for the target vehicle of this study. Finally, the centrifugal force applied to a turning vehicle is expressed as follows in terms of the vehicle mass m_t, vehicle speed V, wheelbase distance L, steering wheel angle δ_s, and steering ratio i_s.

$$F = \frac{m_t V^2 \delta_s}{i_s L} \tag{7}$$

Next, a dynamic vehicle model with seven degrees of freedom was established to analyze the behavior of a driving vehicle. As shown in Figure 2, the vehicle was modeled with one sprung mass and four unsprung masses, with a total of five rigid bodies, and the suspension, anti-roll bar, and tires were modeled as springs and dampers. In Figure 2, the vehicle's forward direction is the negative x-axis direction. In addition, the y- and z-axes are parallel to the left and right directions and up and down directions of the vehicle, respectively. The sprung mass is the total mass of a vehicle supported by the suspension, which includes the body, frame, engine, transmission, and internal components. The unsprung mass includes wheel axles, wheel bearings, wheel hubs, tires, drive shafts, springs, shock absorbers, and suspension links. The motion of the sprung mass is described by the bounce displacement of the mass center Z, the pitch angle φ, and the roll angle θ, while the motions of the unsprung masses are described by the vertical displacements of z_1, z_2, z_3 and z_4. In this study, the x-direction motion of the sprung mass is defined as a constant vehicle speed V, and because the vibration and yaw motion in the x and y directions are ignored, the motion of the sprung mass is defined by the bounce displacement, pitch angle, and roll angle.

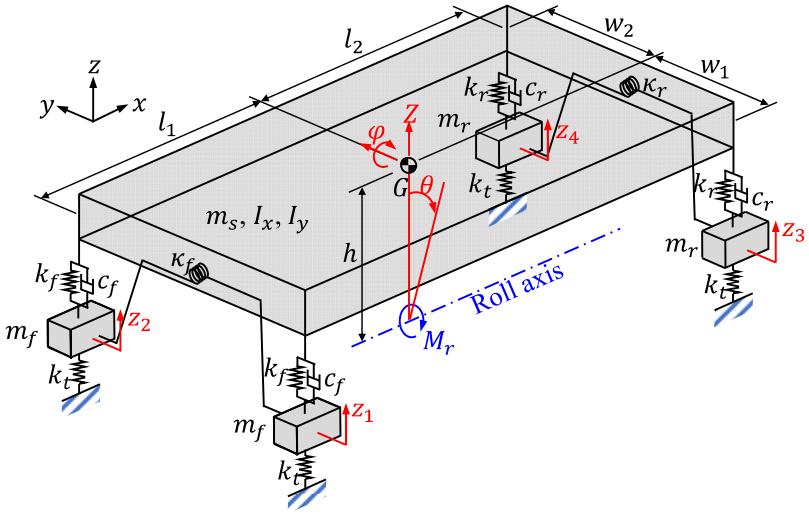

Figure 2. Dynamic model of vehicle with seven degrees of freedom.

As shown in Figure 2, the sprung mass has a roll motion that rotates about a roll axis parallel to the x-axis at a distance $h = 476$ mm vertically from the center of mass [20]. This considers the phenomenon that the lateral centrifugal force acting on the center of mass of the vehicle body located at a distance h from the roll axis generates a roll moment for the vehicle body when the vehicle turns. The position of the roll axis changes with a very complex mechanism depending on the kinematics of the suspension links; however, in this study, the relative position of the roll axis to the body is considered fixed to establish a simple and efficient model. Therefore, the roll moment M_r shown in Figure 2 is expressed as the product of the centrifugal force F applied to the vehicle and the distance h from the roll axis to the mass center, that is, $M_r = Fh$.

The sprung mass has mass m_s, mass moment of inertia about the center of mass I_x, and mass moment of inertia about the y-axis I_y. The mass center of the sprung mass G is located at a distance $l_1 = 1.07$ m from the front of the vehicle, $l_2 = 1.579$ m from the rear, $w_1 = 0.734$ m from the left end of the vehicle, and $w_2 = 0.824$ m from the right end of the vehicle. The front usprung masses with mass m_f have vertical displacements z_1 and z_2, while the rear unsprung masses with mass m_r

Preprints (www.preprints.org) | NOT PEER-REVIEWED | Posted: 19 April 2023 doi:10.20944/preprints202304.0529.v1

have displacements z_3 and z_4. However, experimentally obtaining the mass and mass moment of inertia values of various parts to calculate the inertia parameters of the model shown in Figure 2 is time consuming and complicated procedure. Therefore, in this study, the inertial values of the sprung and unsprung masses for the dynamic vehicle model were extracted from the 3-D solid model of the vehicle using commercial CAD software, and these values are $m_s = 1568$ kg, $m_f = 47$ kg, $m_r = 31$ kg, $I_x = 719$ kg·m2, and $I_y = 2495$ kg·m². The products of inertia were neglected in this study because they were relatively small.

The suspension, tire, and anti-roll bar that connect the rigid body and ground defined above were modeled with linear equivalent springs and dampers. The front suspensions vertically connected between the sprung mass and front unsprung masses were modeled with an equivalent stiffness k_f and an equivalent damping coefficient c_f, and the rear suspension vertically connected between the sprung mass and rear unsprung masses was modeled with an equivalent stiffness k_r and equivalent damping coefficient c_r. As the tires between the ground and the unsprung masses have very high stiffness, they are modeled with an equivalent stiffness k_t without damping.

On the other hand, anti-roll bars, which help reduce vehicle body roll in fast cornering or on irregular roads, are modeled as torsion springs. The bars are long U-shaped metals with hollow cross sections that join the suspensions on the right and left sides of an axle. They are usually attached to the chassis at two points using rubber bushings. The torsional stiffnesses of the front and rear anti-roll bars were assumed to be κ_f and κ_r, respectively [21]. The twist angles of the anti-roll bars were determined by the angular displacements of the axel shafts relative to the sprung mass. The axle shaft has an angular displacement owing to the difference between the right and left wheels. To help understand this, a dynamic vehicle model viewed from the front is shown in Figure 3 as an example.

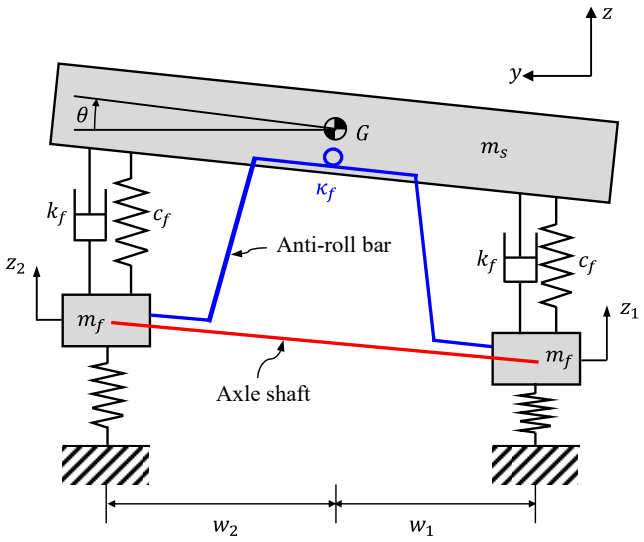

Figure 3. Front view of the dynamic model of vehicle.

As the front left and right unsprung masses have vertical displacements z_1 and z_2, respectively, the angular displacement of the front axle shaft is computed as $\tan^{-1}[(z_2 - z_1)/(w_1 + w_2)]$. Therefore, the twist angle of the front anti-roll bar ϕ_f, is given by

$$\phi_f = \tan^{-1}\left(\frac{z_2 - z_1}{w_1 + w_2}\right) - \theta \tag{8}$$

Similarly, the twist angle of the rear anti-roll bar can be expressed as

$$\phi_r = \tan^{-1}\left(\frac{z_4 - z_3}{w_1 + w_2}\right) - \theta \tag{9}$$

The equivalent stiffness and damping coefficients presented above were calculated using an experimental method. The equivalent stiffness values of the suspensions and tires were obtained through static vertical load-deflection tests [22,23], and similarly, the equivalent torsional stiffness

Preprints (www.preprints.org) | NOT PEER-REVIEWED | Posted: 19 April 2023 doi:10.20944/preprints202304.0529.v1

values of the anti-roll bars were obtained through torsional load-torsion angular deformation tests. The values for the various equivalent stiffness, equivalent torsional stiffness, and damping coefficients obtained by the tests were as follows: $k_f = 44400$ N/m, $k_r = 36000$ N/m, $k_t = 255487$ N/m, $\kappa_f = 62085$ N·m/rad, $\kappa_r = 58098$ N·m/rad, and $c_f = c_r = 5000$ N·s/m.

The equations of motion for the driving vehicle were derived using the following Lagrange equation:

$$\frac{\mathrm{d}}{\mathrm{dt}}\left(\frac{\partial T}{\partial \dot{q}_k}\right) + \frac{\partial F_d}{\partial \dot{q}_k} - \frac{\partial T}{\partial q_k} + \frac{\partial V}{\partial q_k} = Q_k \quad \text{for } k = Z, \theta, \varphi, z_1, z_2, z_3, z_4 \tag{10}$$

where the superposed dot represents differentiation with respect to time; q_k stands for the seven generalized coordinates; T, V, F_d and Q_k are the kinetic energy, potential energy, Rayleigh's dissipation function, and generalized force, respectively. Among the generalized coordinates, the three coordinates (Z, θ, and φ) are for the motion of the sprung mass, whereas the four coordinates (z_1, z_2, z_3, z_4) are for the motions of the unsprung masses.

First, the kinetic energy of the dynamic vehicle model can be expressed as the following equation:

$$T = \frac{1}{2}m_s\left(V^2 + \dot{Z}^2\right) + \frac{1}{2}I_x\dot{\theta}^2 + \frac{1}{2}I_y\dot{\varphi}^2 + \frac{1}{2}m_f(\dot{z}_1^2 + \dot{z}_2^2) + \frac{1}{2}m_r(\dot{z}_3^2 + \dot{z}_4^2) \tag{11}$$

where the first term is for the translational motion of the sprung mass, the second and third terms are for the rotational motion of the sprung mass, and the fourth and fifth terms are for the translational motions of the unsprung masses.

Next, the potential energy owing to the deformations of the springs and torsional springs in the dynamic vehicle model may be given by

$$V = \frac{1}{2}k_t\sum_{i=1}^{4} z_i^2 + \frac{1}{2}k_f(d_1^2 + d_2^2) + \frac{1}{2}k_r(d_3^2 + d_4^2) + \frac{1}{2}\kappa_f\phi_f^2 + \frac{1}{2}\kappa_r\phi_r^2 \tag{12}$$

where the first term is the potential energy of the tire, the second and third terms are the potential energies of the suspensions, and the fourth and fifth terms are the potential energies of the anti-roll bars. In the second and third terms, d_1, d_2, d_3, and d_4 are the suspension deformations at the left front wheel, right front wheel, left rear wheel, and right rear wheel, respectively.

The suspension deformation at each wheel, d_i for i=1, 2, 3, 4, is determined by subtracting the displacement of the unsprung mass from the z-directional displacement of the sprung mass at the point corresponding to each suspension. The displacement of the sprung mass at the left-front suspension, $\mathbf{x}_1$, displacement at the right-front suspension, $\mathbf{x}_2$, displacement at the left-rear suspension, $\mathbf{x}_3$, and displacement at the right-rear suspension, $\mathbf{x}_4$, can be determined by

$$\mathbf{x}_i = \mathbf{x}_G + \mathbf{T}_\varphi\mathbf{T}_\theta\mathbf{P}_i \quad \text{for } i = 1, 2, 3, 4 \tag{13}$$

where $\mathbf{x}_G$ is the displacement of the mass center of the sprung mass, $\mathbf{P}_i$ is the position vector of the point on the spring mass corresponding to each suspension, and $\mathbf{T}_\theta$ and $\mathbf{T}_\varphi$ are the rotation matrices about the x and y axes, respectively. The vectors and matrices in Equation (13) are given by

$$\mathbf{x}_G = \begin{Bmatrix}0\\0\\Z\end{Bmatrix},\ \mathbf{P}_1 = \begin{Bmatrix}-l_1\\-w_1\\0\end{Bmatrix},\ \mathbf{P}_2 = \begin{Bmatrix}-l_1\\w_2\\0\end{Bmatrix},\ \mathbf{P}_3 = \begin{Bmatrix}l_2\\-w_1\\0\end{Bmatrix},\ \mathbf{P}_4 = \begin{Bmatrix}l_2\\w_2\\0\end{Bmatrix} \tag{14}$$

$$\mathbf{T}_\theta = \begin{bmatrix}1 & 0 & 0\\0 & \cos\theta & \sin\theta\\0 & -\sin\theta & \cos\theta\end{bmatrix},\ \mathbf{T}_\varphi = \begin{bmatrix}\cos\varphi & 0 & -\sin\varphi\\0 & 1 & 0\\\sin\varphi & 0 & \cos\varphi\end{bmatrix} \tag{15}$$

Preprints (www.preprints.org) | NOT PEER-REVIEWED | Posted: 19 April 2023 doi:10.20944/preprints202304.0529.v1

In other words, the suspension deformations were obtained by subtracting the displacements of the corresponding unsprung mass z_i from the z-directional components of $\mathbf{x}_i$. Consequently, the suspension deformations can be expressed as

$$\begin{aligned} d_1 &= Z - z_1 - w_1\sin\theta\cos\varphi + l_1\sin\varphi,\ d_2 = Z - z_2 + w_2\sin\theta\cos\varphi + l_1\sin\varphi, \\ d_3 &= Z - z_3 - w_1\sin\theta\cos\varphi - l_2\sin\varphi,\ d_4 = Z - z_4 + w_2\sin\theta\cos\varphi - l_2\sin\varphi \end{aligned} \tag{16}$$

On the other hand, Rayleigh's dissipation function for the vehicle model can be represented by

$$F_d = \frac{1}{2}c_f\left(\dot{d}_1^2 + \dot{d}_2^2\right) + \frac{1}{2}c_r\left(\dot{d}_3^2 + \dot{d}_4^2\right) \tag{17}$$

where $\dot{d}_i$ $(i = 1,\ 2,\ 3,\ 4)$ are the time derivatives of the suspension deformations given by Equation (16). Finally, the non-conservative generalized forces of Equation (10) are given by

$$Q_\theta = M_r,\quad Q_Z = Q_\varphi = Q_{z_1} = Q_{z_2} = Q_{z_3} = Q_{z_4} = 0 \tag{18}$$

As shown in these equations, there are no generalized forces except for Q_θ, and this generalized force Q_θ is the roll moment described above.

The equations of motion were obtained by substituting the kinetic energy (Equation (11)), potential energy (Equation (12)), Rayleigh's dissipation function (Equation (17)), and generalized forces (Equation (18)) into Lagrange equation (Equation (10)). The derived equations are nonlinear ordinary differential equations for generalized coordinates. Assuming that the roll and pitch angles are small, the nonlinear equation can be linearized the linearized equations of motion can be written as a matrix-vector equation, as follows:

$$\mathbf{M}\ddot{\mathbf{q}} + \mathbf{C}\dot{\boldsymbol{q}} + \mathbf{K}\mathbf{q} = \mathbf{f} \tag{19}$$

where the superposed dot represents differentiation with respect to time, $\mathbf{q}$ is the displacement vector defined by $\mathbf{q}$=$\{\theta,\ \varphi,\ Z,\ z_1,\ z_2,\ z_3,\ z_4\}^{\mathrm{T}}$, $\mathbf{M}$ is the mass matrix, $\mathbf{C}$ is the damping matrix, $\mathbf{K}$ is the stiffness matrix, and $\mathbf{f}$ is the load vector defined by $\mathbf{f} = \{M_r, 0, 0, 0, 0, 0, 0\}^{\mathrm{T}}$.

3. Dynamics Model Verification

To verify the dynamic vehicle model proposed in this study, the vertical suspension deformations computed using the vehicle model were compared with the deformations measured through actual vehicle driving tests. The vehicle for the driving tests was a semi-midsize hatchback-type passenger car with specifications mentioned above. This vehicle, with one driver on board, was driven at a constant speed of 100 km/h on an outdoor proving ground with a dry and flat road surface. Three types of driving tests were conducted: slalom, double lane change, and step steer test. These tests are performed for three steering wheel angle variations, the details of which will be discussed later.

The experimental setup for measuring the suspension deformations is shown in Figure 4. The pedal controller was used to maintain the vehicle speed at 100 km/h. The steering machine provides steering wheel angle variations for driving tests according to the steering wheel angle pattern entered in advance. Four wheel-watch cameras were installed on the exterior of the vehicle to measure the suspension deformations under the dynamic condition of the vehicle. These cameras were mounted on camera mounts that extended approximately 300 mm outward and transversely from the vehicle body on the tops of the four wheels and measured the relative motions of the wheels in the longitudinal, lateral, and vertical directions with respect to the vehicle body. The data on suspension deformations measured by the cameras were stored in the data acquisition module, and a laptop computer was installed to monitor these data in real time.

Preprints (www.preprints.org) | NOT PEER-REVIEWED | Posted: 19 April 2023 doi:10.20944/preprints202304.0529.v1

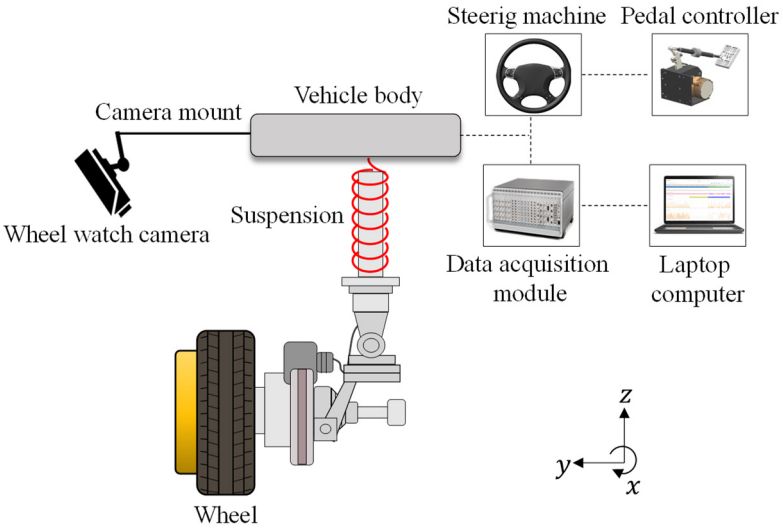

Figure 4. Schematic diagram for the experimental setup for measuring suspension deformations.

First, the suspension deformations were experimentally measured while performing the slalom test and compared with the deformations from the simulation using the dynamic model established in the previous section. For the slalom test, six cones were installed at equal intervals of 45 m on a flat road, and the test vehicle was driven zigzag between the cones at a constant speed of 100 km/h. The steering wheel angle variation for zigzag driving, as shown in Figure 5, was imposed on the vehicle. Note that the positive direction of the steering wheel angle is clockwise.

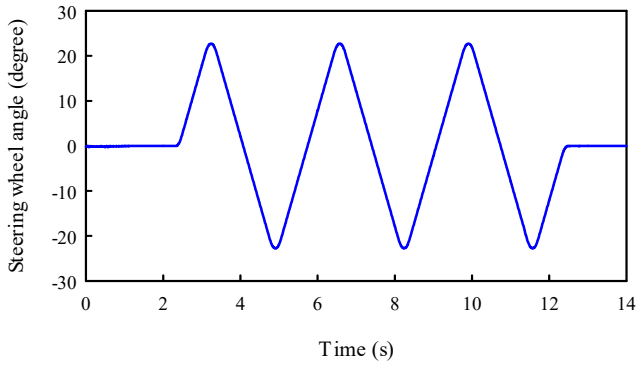

Figure 5. Time variation of the steering wheel angle for the slalom test.

The suspension deformations measured during the slalom test are shown in Figure 6, where Figure 6a shows the deformation at the left front wheel, Figure 6b shows the deformation at the right front wheel, Figure 6c shows the deformation at the left rear wheel, and Figure 6d shows the deformation at the right rear wheel. In this figure, the blue, red, and black lines represent the deformations in the directions of the x, y, and z axes, respectively, which are the forward-rearward, left-right, and down-up directions with respect to the vehicle. The vertical deformations of the left suspensions of the vehicle (Figure 6a and 6c) have opposite phases to those of the right suspensions (Figure 6b and Figure 6d). This is because the vehicle body rolls about the x-axis during turning, causing compressive deformation on the left side of the suspensions and tensile deformation on the right side. The deformations in the z-direction are much larger than those in the x- and y-directions. This implies that the suspensions, which are connected in a nearly vertical position between the wheels and body, are vertically tensioned or compressed. Therefore, only the z-directional suspension deformations were considered in the comparison between the simulation and experimental results.

Preprints (www.preprints.org) | NOT PEER-REVIEWED | Posted: 19 April 2023 doi:10.20944/preprints202304.0529.v1

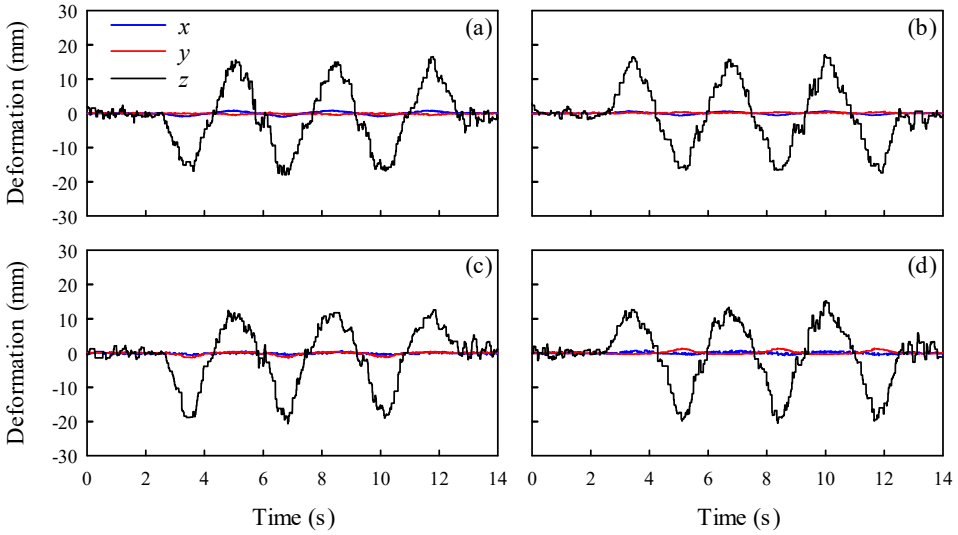

Figure 6. Suspension deformations measured during the slalom test: (a) at the left front wheel; (b) at the right front wheel; (c) at the left rear wheel; and (d) at the right rear wheel.

Simulations were performed with the dynamic vehicle model expressed as the equations of motion derived in the previous section. After obtaining the roll moment M_r using the centrifugal force computed with the steering wheel angle for the slalom test shown in Figure 5, it was substituted into the equations of motion given by Equation (19). Applying the Newmark time integration method [24] with a time step size of 0.005 s to the equations of motion, the time histories of the bounce displacement (Z), pitch angle (φ), roll angle (θ), and vertical displacements of the unsprung masses (z_1, z_2, z_3, z_4) were computed. Using these time histories, the vertical suspension deformations at the four wheels were computed from the following linearized deformations:

$$d_1 = Z - z_1 - w_1\theta + l_1\varphi,\ d_2 = Z - z_2 + w_2\theta + l_1\varphi,$$
$$d_3 = Z - z_3 - w_1\theta - l_2\varphi,\ d_4 = Z - z_4 + w_2\theta - l_2\varphi \quad (20)$$

The dynamic responses of the suspension deformations by simulation and experiment during the slalom test for 14 s are shown in Figure 7, where Figures 7a–d are for the left front, right front, left rear, and right rear wheels, respectively. In this figure, the red and blue solid lines represent the simulated and experimental results, respectively. Figure 7 shows that the overall behaviors of the simulation are very close to the behaviors of the experiment. This implies that the vehicle dynamics model presented in this study can be used to predict the behavior of a vehicle during a slalom test. However, the experimental results for the suspension deformations at all wheels had high-frequency vibrations compared with the simulation results. This is because, unlike the vehicle dynamic model, real vehicles have high-frequency components of vibration in suspension deformations. These high-frequency components are caused by the wheel vibrations owing to the uneven road surface and the vibrations of various power transmission system components.

Preprints (www.preprints.org) | NOT PEER-REVIEWED | Posted: 19 April 2023 doi:10.20944/preprints202304.0529.v1

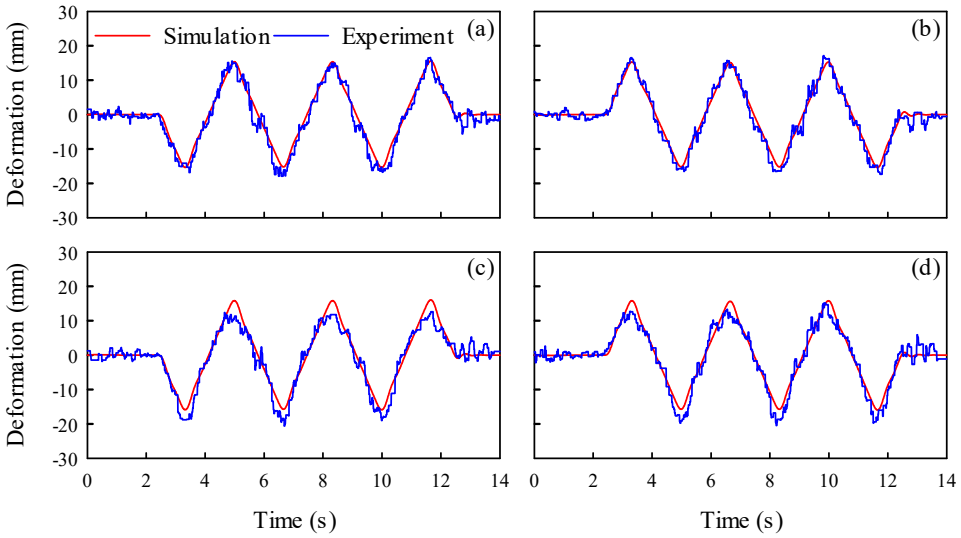

Figure 7. Comparison of the vertical suspension deformations during the slalom test between the simulation and experiment: (a) at the left front wheel; (b) at the right front wheel; (c) at the left rear wheel; and (d) at the right rear wheel.

Next, while the steering wheel angle shown in Figure 8 was imposed on the vehicle, the suspension deformations were measured during the double lane change test. These measured deformations were compared with the simulated deformations to validate the vehicle dynamic model. The double-lane change test was performed by maintaining the vehicle speed constant at 100 km/h. Similar to the slalom test, the suspension deformations in the horizontal directions of the vehicle (x and y directions) were very small compared to the deformations in the vertical direction (the z direction); therefore, the deformations in only the vertical direction were compared between the simulation and the experiment.

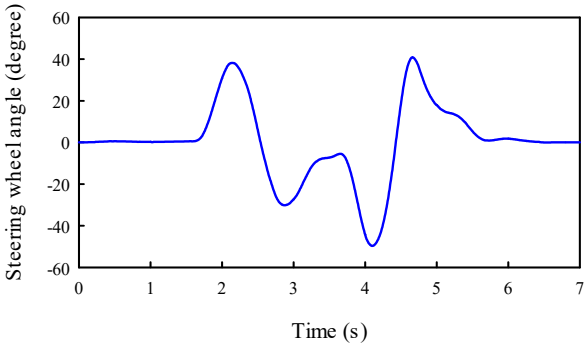

Figure 8. Time variation of the steering wheel angle for the double lane change test.

Figure 9 compares the results of the simulation and experiment for suspension deformations during the 7-second double lane change test. The suspension deformations at the four wheels are shown in Figures 9a–d, where the red and blue lines represent the simulation and experiment results, respectively. For the double-lane change test, the suspension deformations obtained by simulation using the vehicle dynamic model presented in this study follow the deformations measured through the experiment. However, slightly larger overshoots are observed in the simulation results compared to the experimental results at approximately 4.09 s in Figures 9a and 9c and approximately 2.08 s in Figure 9d. This implies that the simplified and linearized vehicle dynamic model proposed in this study does not sufficiently reflect the complex kinematic and nonlinear elements of an actual vehicle. Nevertheless, the suggested model simulates the overall vehicle behavior relatively well while performing the double-lane change test.

Preprints (www.preprints.org) | NOT PEER-REVIEWED | Posted: 19 April 2023 doi:10.20944/preprints202304.0529.v1

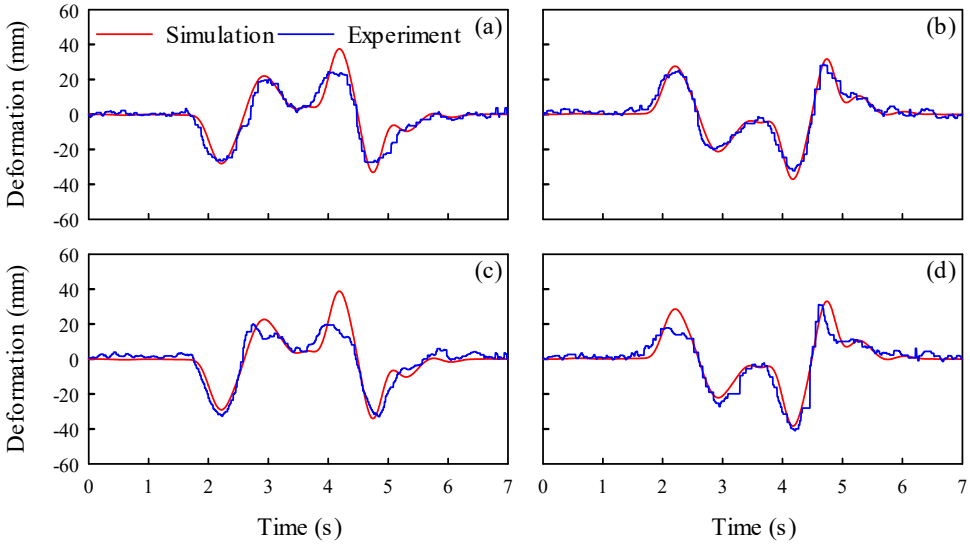

Figure 9. Comparison of the vertical suspension deformations during the double lane change test between the simulation and experiment: (a) at the left front wheel; (b) at the right front wheel; (c) at the left rear wheel; and (d) at the right rear wheel.

Finally, during the step steer test, the vehicle model was verified again by comparing the suspension deformations measured on the actual vehicle in motion with the deformations calculated in the simulation using the presented model. The step steer test, often referred to as the J-turn test, involves applying a fast steering-wheel input to a fixed magnitude of the steering wheel angle while the vehicle moves along a straight path at a constant speed. While maintaining the vehicle speed at 100 km/h, the steering wheel angle, shown in Figure 10, was imposed on the vehicle.

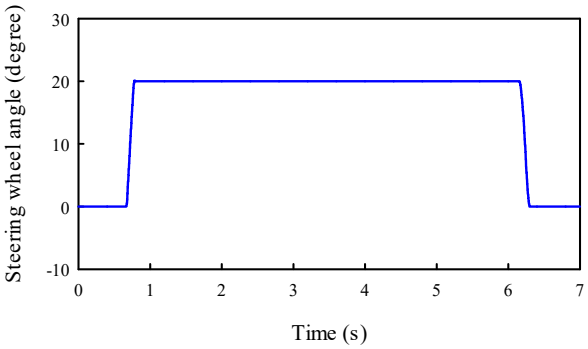

Figure 10. Time variation of the steering wheel angle for the step steer test.

The suspension deformations for the step steer test by simulation and measurement are shown in Figure 11. This figure shows that the suspension deformations obtained by the simulation, indicated by the red line, were in good overall agreement with the deformations measured by the experiment, indicated by the blue line. The high-frequency components in the time responses of suspension deformations, which were shown in the experimental results of the slalom test above, were also observed in the experimental results of the step steer test. Consequently, the simulations using the vehicle dynamic model proposed in this study provide reasonable computations of the suspension deformations for the three tests: the slalom, double lane change, and step steer.

Preprints (www.preprints.org) | NOT PEER-REVIEWED | Posted: 19 April 2023 doi:10.20944/preprints202304.0529.v1

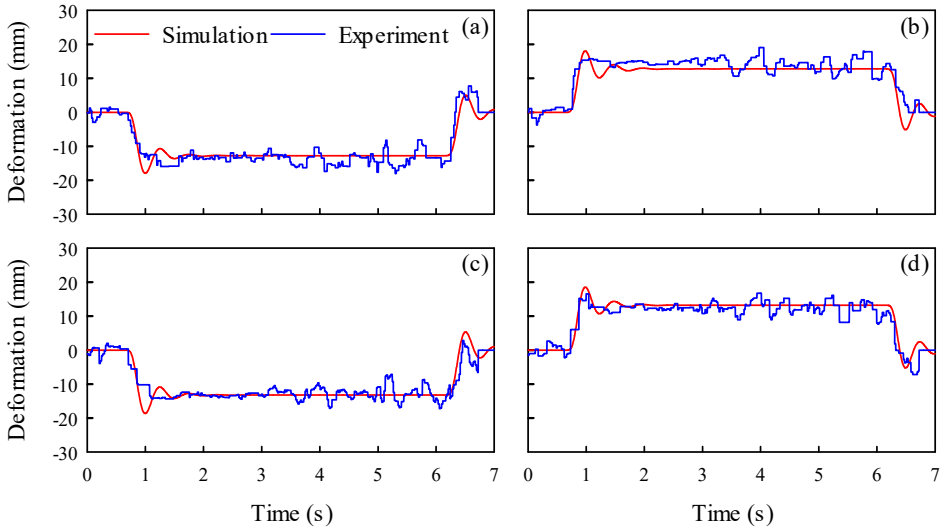

Figure 11. Comparison of the vertical suspension deformations during the step steer test between the simulation and experiment: (a) at the left front wheel; (b) at the right front wheel; (c) at the left rear wheel; and (d) at the right rear wheel.

4. Dynamic Analysis

4.1. Natural Frequencies and Mode Shapes

Consider the natural frequencies and mode shapes of the dynamic vehicle model developed in Section 2, the natural frequency and mode shape were computed from the eigenvalue problem obtained by ignoring the damping term on the left and force term on the right in Equation (19). As the damping properties have little influence on the natural frequencies, the damping term is negligible. Assuming $\mathbf{q} = \mathbf{Q}e^{j\omega t}$ where $j = \sqrt{-1}$, ω is the natural frequency, and $\mathbf{Q}$ is the modal vector, the eigenvalue problem is given by

$$(\mathbf{K}-\omega^2\mathbf{M})\mathbf{Q} = \mathbf{0} \tag{21}$$

As the proposed model has seven degrees of freedom, the number of acquired natural frequencies and corresponding mode shapes is seven. The computed natural frequencies are 1.44, 1.62, 1.99, 12.73, 13.78, 15.45, and 16.67 Hz. The obtained mode shapes for these natural frequencies are displayed in Figures 12 and 13, which show the mode shapes for the sprung and unsprung masses, respectively. In these figures, the dashed lines represent the positions where each mass does not move, and the solid lines represent the mode shapes where each mass moves.

The mode shapes of the sprung mass are shown in Figure 12. The bounce mode is for a vertical motion of the sprung mass, the pitch is for a rotation about the y axis, and the roll mode is for a rotation about the x axis. However, because the two modes shown in Figures 12a and 12b are modes in which bounce and pitch motions are combined, it is difficult to clearly distinguish these two modes as the bounce and pitch modes. In the mode shown in Figure 12a, bounce motion is more dominant than pitch motion. In contrast, the mode shown in Figure 12b has more pitch motion than bounce motion. In this study, the two modes with combined bounce and pitch motions, shown in Figures 12a and 12b, are called bounce-pitch modes. Comparing Figures 12a and 12b, the mode in Figure 12c has a distinct roll motion, indicating that it is a roll mode. The natural frequencies for the bounce-pitch modes are 1.44 and 1.62 Hz, and the natural frequency for the roll mode is 1.99 Hz.

Preprints (www.preprints.org) | NOT PEER-REVIEWED | Posted: 19 April 2023 doi:10.20944/preprints202304.0529.v1

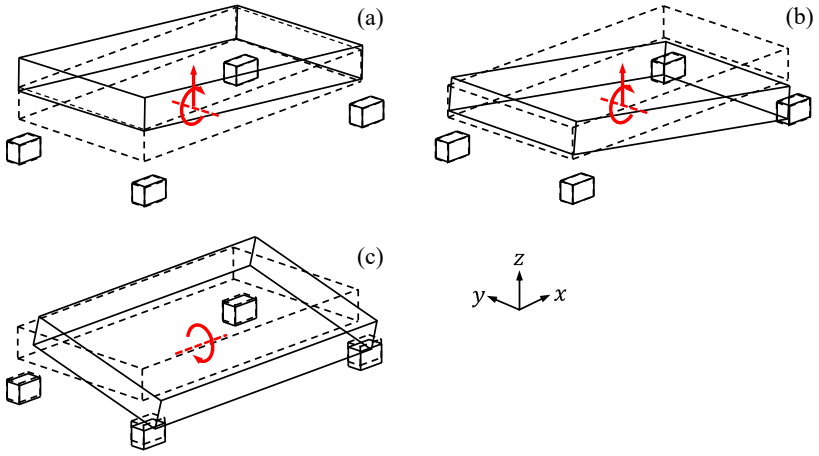

Figure 12. Mode shapes of the sprung mass: (a) the bounce-pitch mode with natural frequency of 1.44 Hz; (b) the bounce-pitch mode with natural frequency of 1.62Hz; and (c) the roll mode with natural frequency of 1.99 Hz.

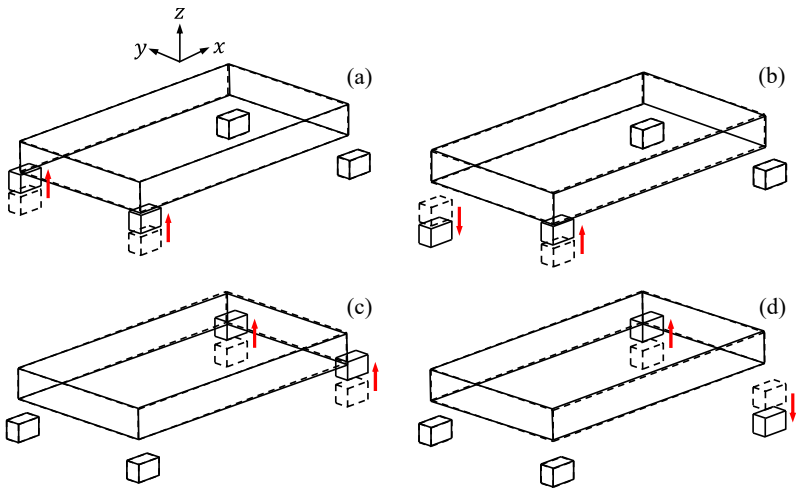

Figure 13. Mode shapes of the unsprung mass: (a) the in-phase front wheel mode (12.73 Hz); (b) the out-of-phase front wheel mode (13.78 Hz); (c) the in-phase rear wheel mode (15.45 Hz); and (d) the out-of-phase rear wheel mode.

The mode shapes of the unsprung masses are displayed in Figure 13, where Figures 13a-d show the in-phase front wheel mode, out-of-phase front wheel mode, in-phase rear wheel mode, and out-of-phase rear wheel mode, respectively. In the in-phase front wheel mode with a natural frequency of 12.73 Hz, the two front wheels vibrate in the same direction, but the rear wheels are motionless (Figure 13a). On the other hand, the out-of-phase front wheel mode with a natural frequency of 13.78 Hz has vibrations of the front wheels with opposite directions and no motion in the rear wheels (Figure 13b). Similarly, in the in-phase rear wheel mode with a natural frequency of 15.42 Hz, the rear wheels vibrate in the same direction (Figure 13c), and in the out-of-phase rear wheel mode with a natural frequency of 16.67 Hz, the rear wheels vibrate in opposite directions (Figure 13d). Note that the natural frequencies of the vibration modes related to sprung masses are much lower than those of the vibration modes related to unsprung masses.

We analyzed the effects of the vehicle suspension stiffness and anti-roll bar torsional stiffness on the natural frequencies for the sprung and unsprung modes. The natural frequencies for the change in stiffness are shown in Figures 14-19, where the abscissa represents the front suspension stiffness, while the ordinate represents the natural frequency. The numbers on the abscissa indicate the multiples of the stiffness given in Section 2. For example, '0.1' on the abscissa of Figure 14 means 0.1 times k_f, which is the front suspension stiffness of $0.1k_f$. In Figures 14-19, the hollow inverted triangles represent the natural frequencies of the two bounce-pitch modes of the sprung mass. These

Preprints (www.preprints.org) | NOT PEER-REVIEWED | Posted: 19 April 2023 doi:10.20944/preprints202304.0529.v1

inverted triangles are not connected by lines because the bounce and pitch modes are not clearly distinguished and are mixed, as previously explained. The natural frequencies for the roll mode of the sprung mass are shown as blue triangles connected by solid blue lines. The natural frequencies for the in-phase front wheel mode, out-of-phase front wheel mode, in-phase rear wheel mode, and out-of-phase rear wheel mode are represented by hollow squares with solid lines, hollow circles with red dotted lines, hollow triangles with solid lines, and blue crosses with blue dotted lines, respectively.

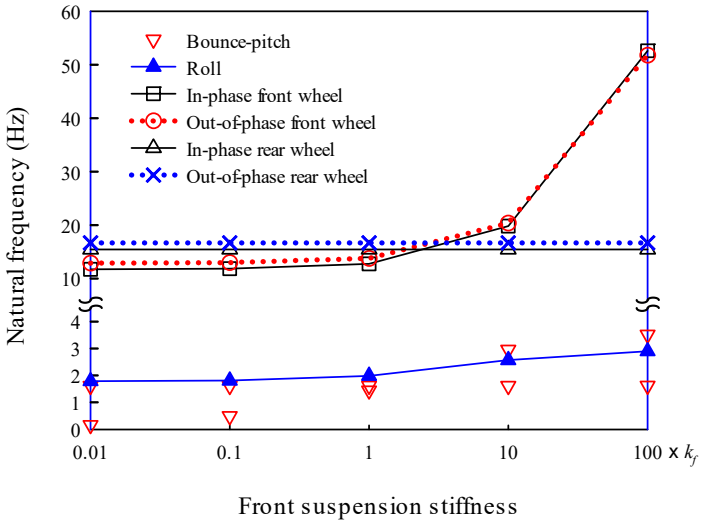

Figure 14. Natural frequencies for the variation of the front suspension stiffness.

First, we consider the effect of suspension stiffness variation on the natural frequencies of the modes. Figure 14 shows the natural frequencies for the values of the front suspension stiffness, $0.01k_f$, $0.1k_f$, k_f, $10k_f$, and $100k_f$, where $k_f = 44400$ N/m, as given in Section 2. The dimensions and material properties of the vehicle model, excluding the front suspension stiffness, were the same as those presented in Section 2. As shown in the figure, the natural frequencies of the sprung mass modes were much lower than those of the unsprung mass modes. The natural frequencies for the bounce-pitch modes of the sprung mass are 0.16 and 1.61 Hz for $0.01k_f$, 0.49 and 1.61 Hz for $0.1k_f$, 1.44 and 1.62 Hz for k_f, 1.61 and 2.95 Hz for $10k_f$, and 1.62 and 3.51 Hz for $100k_f$. Notably, one of the natural frequencies for the bounce-pitch modes does not change significantly and remains close to 1.61 Hz. Other natural frequencies not close to 1.61 Hz increase to 0.16, 0.49, 1.44, 2.95, and 3,51 Hz as the suspension stiffness increases. As observed in this figure that the natural frequencies for the roll mode of the sprung mass, as well as the in-phase and out-of-phase front wheel modes, increase with the front suspension stiffness. However, the natural frequencies of the in-plane and out-of-plane rear-wheel modes remained constant even as the front suspension stiffness increased. In other words, the front suspension stiffness affects the natural frequencies of the front-wheel modes but not the frequencies of the rear-wheel modes.

The changes in the natural frequencies of the dynamic vehicle model are presented in Figure 15 when the rear suspension stiffness is varied from $0.01k_r$ to $100k_r$ while the front suspension stiffness is fixed at k_f. Similar to Figure 14, one of the natural frequencies for the bounce-pitch modes increases and the others remain constant around 1.45 Hz as the rear suspension stiffness increases. The natural frequency for the roll mode also increased with the rear suspension stiffness. However, when the rear suspension stiffness increases, the natural frequencies of the rear wheel modes increase, while the natural frequencies of the front wheel modes remain constant. It can be concluded from Figures 14 and 15 that if one of the front and rear wheel suspension stiffnesses increases, the natural frequencies for the roll mode, associated wheel modes, and one of the bounce-pitch modes increase, while the frequencies of the other modes remain constant. Figure 16 shows the changes in natural frequencies when the stiffnesses of both the front and rear suspensions increase

Preprints (www.preprints.org) | NOT PEER-REVIEWED | Posted: 19 April 2023 doi:10.20944/preprints202304.0529.v1

simultaneously from 0.01 times to 100 times the stiffness values given in Section 2. In this case, as expected, the natural frequencies for all modes for the sprung and unsprung masses increased.

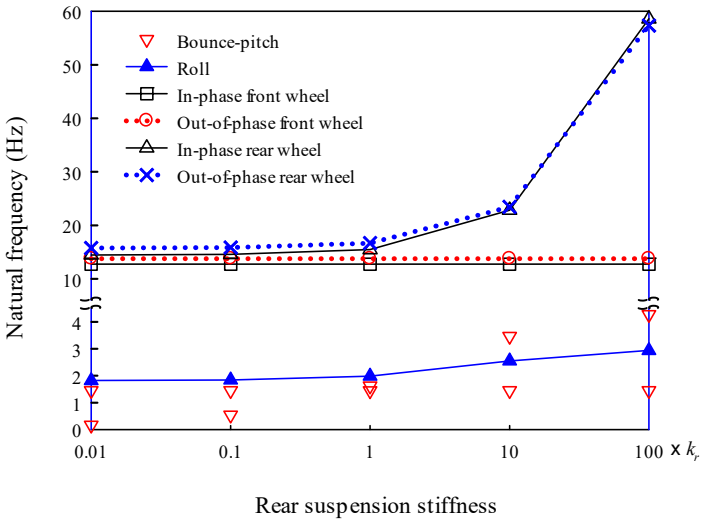

Figure 15. Natural frequencies for the variation of the rear suspension stiffness.

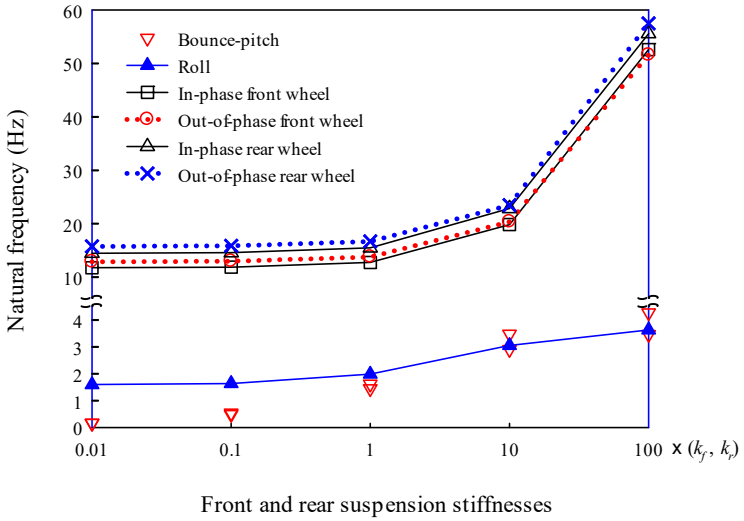

Figure 16. Natural frequencies when the front and rear suspension stiffnesses change simultaneously.

Next, we analyzed the effects of changes in the torsional stiffness of the front anti-roll bar on the natural frequencies of the vehicle model. Using the torsional stiffness of the front anti-roll bar $\kappa_f = 62085$ N·m/rad as a reference value, the natural frequencies were computed for five torsional stiffness values of 0.01, 0.1, 1, 10, and 100 times κ_f. The computed results are shown in Figure 17. As shown in this figure, the natural frequency for the roll mode of the sprung mass increases with the torsional stiffness of the front anti-roll bar; however, the natural frequencies for the bounce-pitch modes remain unchanged, regardless of the torsional stiffness. Among the natural frequencies for the modes of unsprung masses, only the natural frequency for the out-of-phase front wheel mode increases with the torsional stiffness, while the natural frequencies of other modes remain unchanged.

Preprints (www.preprints.org) | NOT PEER-REVIEWED | Posted: 19 April 2023 doi:10.20944/preprints202304.0529.v1

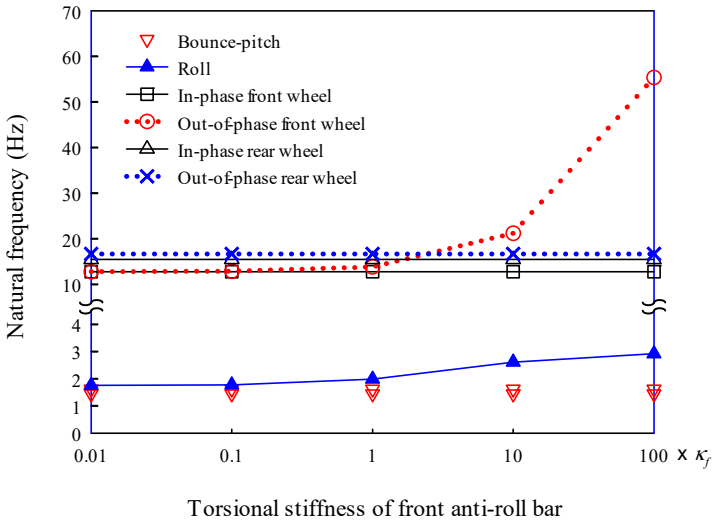

Figure 17. Natural frequencies for the variation of the torsional stiffness of the front anti-roll bar.

Figure 18 shows the change in the natural frequencies of the dynamic vehicle model when the torsional stiffness of the rear anti-roll bar is increased. The natural frequencies were computed while increasing the torsional stiffness of the rear anti-roll bar from $0.01\kappa_r$ to $100\kappa_r$ with all other dimensions and material properties fixed. The value of κ_r is 58098 N·m/rad, as given in Section 2. As shown in Figure 18, the natural frequencies of the sprung mass roll mode and out-of-phase rear wheel mode increased with the torsional stiffness of the rear anti-roll bar. However, this change in torsional stiffness had no effect on the natural frequencies of the other modes. It is observed from Figures 17 and 18 that if only one of the two anti-roll bar torsional stiffnesses increases, the natural frequencies of the roll mode and the corresponding out-of-phase wheel mode increase, while the natural frequencies of the other modes remain unchanged.

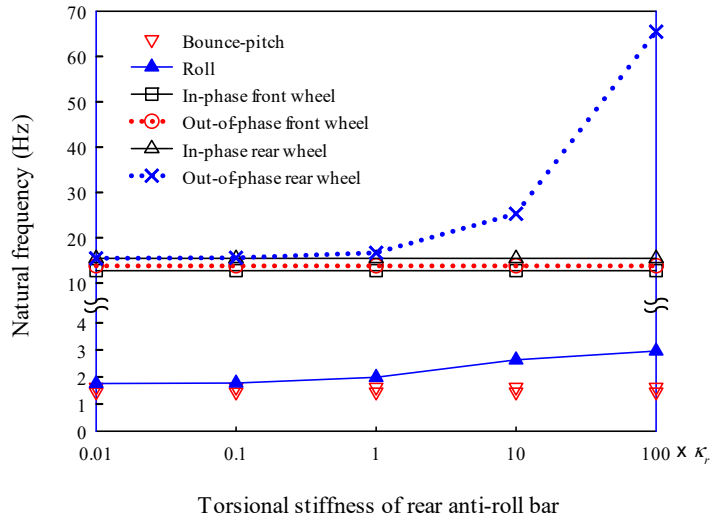

Figure 18. Natural frequencies for the variation of the torsional stiffness of the rear anti-roll bar.

Figure 19 shows the changes in natural frequencies of the vehicle model when the torsional stiffnesses of the front and rear anti-roll bars increased simultaneously. The natural frequencies in this figure were computed with values of 0.01, 0.1, 1, 10, and 100 times the values of κ_f and κ_r presented in Section 2. As shown in this figure, the natural frequencies of the bounce-pitch modes and in-phase wheel modes remain unchanged even when the torsional stiffness increases. However,

Preprints (www.preprints.org) | NOT PEER-REVIEWED | Posted: 19 April 2023 doi:10.20944/preprints202304.0529.v1

the natural frequencies of the roll mode and out-of-phase wheel modes increase with torsional stiffness. Comparing Figures 17–19, the result of simultaneously increasing the front and rear torsional stiffnesses (Figure 19) is a combination of the result of increasing the front torsional stiffness (Figure 17) and rear torsional stiffness (Figure 18). Therefore, the natural frequency of the roll mode in Figure 19 is higher than the natural frequencies of the roll modes shown in Figures 17 and 18.

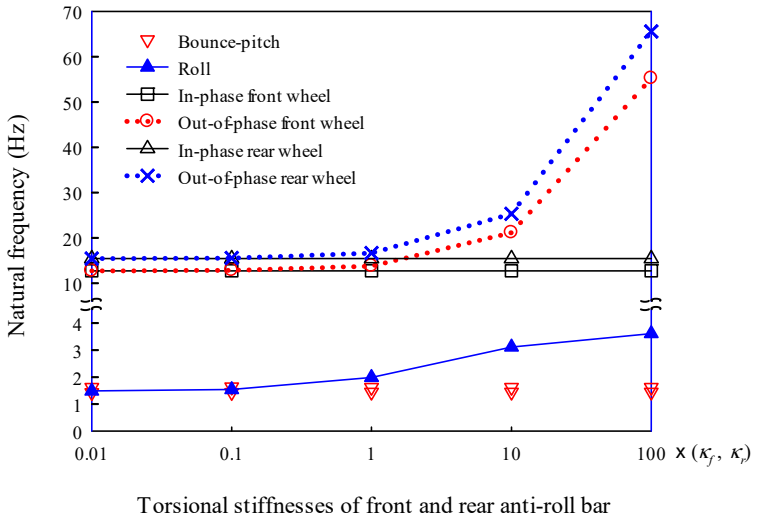

Figure 19. Natural frequencies when the torsional stiffnesses of the front and rear anti-roll bars change simultaneously.

The suspension deformations for the step steer test by simulation and measurement are shown in Figure 11. This figure shows that the suspension deformations obtained by the simulation, indicated by the red line, were in good overall agreement with the deformations measured by the experiment, indicated by the blue line. The high-frequency components in the time responses of suspension deformations, which were shown in the experimental results of the slalom test above, were also observed in the experimental results of the step steer test. Consequently, the simulations using the vehicle dynamic model proposed in this study provide reasonable computations of the suspension deformations for the three tests: the slalom, double lane change, and step steer.

4.2. Dynamic Responses

We analyzed the effects of changes in the design parameters on the dynamic response of the vehicle model. In this study, the suspension stiffness, suspension damping, and anti-roll bar torsional stiffness, which are relatively easy to change, were selected as the design parameters related to dynamic responses. The sprung mass, mass moment of inertia for the sprung mass, unsprung mass, and tire stiffness are not considered as design parameters because their design changes are difficult. To obtain the dynamic responses of the vehicle model, simulations were performed for the step steer test with the steering wheel angle shown in Figure 10 and a vehicle speed of 100 km/h. The reason for selecting the dynamic responses for the step steer test is that the step steer test provides a much harsher driving condition than the slalom and double-lane tests. Therefore, the dynamic responses to the step steer test have been analyzed in many studies [25–27]. When the step steer test is performed, the dynamic response to the pitch angle is much smaller than the dynamic response to the bounce displacement and roll angle. Therefore, in this study, the dynamic responses for the bounce and roll, excluding the pitch, are analyzed.

First, the effects of suspension stiffness on the dynamic response of the sprung mass bounce and roll were investigated. The dynamic responses of the bounce displacement and roll angle for the step steer test are shown in Figure 20. These responses were computed for the three sets of front and rear suspension stiffnesses: $(0.1k_f,\ 0.1k_r)$, $(k_f,\ k_r)$, and $(10k_f,\ 10k_r)$, where the values of k_f and k_r are the same as those presented in Section 2.

Preprints (www.preprints.org) | NOT PEER-REVIEWED | Posted: 19 April 2023 doi:10.20944/preprints202304.0529.v1

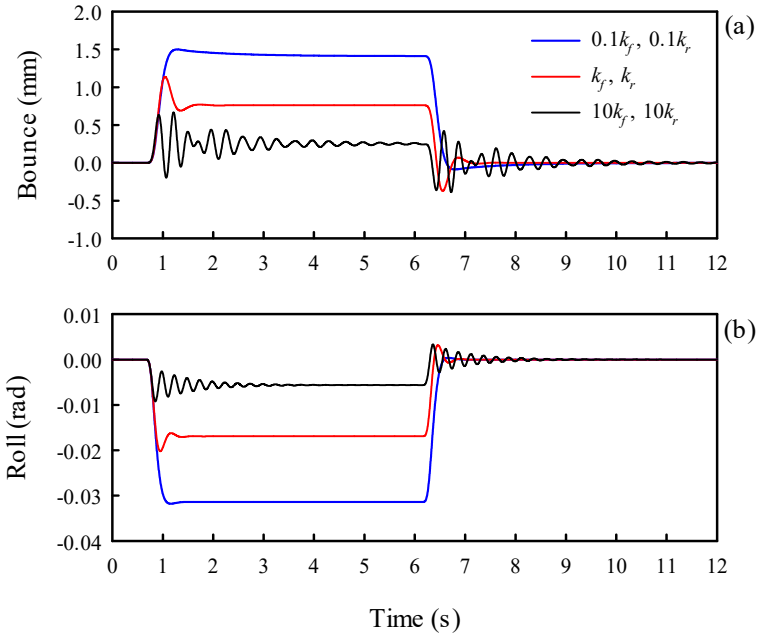

Figure 20. Dynamic responses of the displacements for three values of the suspension stiffness: (a) the bounce and (b) the roll.

As shown in Figure 20a, a positive bounce displacement occurs when the steering wheel angle of Figure 10 is given to the vehicle model. As shown in this figure, the bounce displacement is large when the suspension stiffness is low (in the case of $0.1k_f$ and $0.1k_r$) and is small when the stiffness is high (in the case of $10k_f$ and $10k_r$). However, Figure 20b shows that the roll angles obtained by this step steer test have negative values and become larger as the suspension stiffness decreases. The negative roll angle was caused because a positive steering wheel angle moves the left side of the sprung mass down and the right side up, as shown in Figure 11, resulting in a negative roll angle. Notably, the bounce displacement and roll angle, shown as solid black lines, exhibit high-frequency oscillations when the suspension stiffness is large. The high-frequency oscillation period of the bounce displacement was approximately 0.292 s, and the oscillation period of the roll angle was approximately 0.250 s. These periods correspond to frequencies of 3.42 and 4.00 Hz. The natural frequencies of the bounce-pitch modes are 2.93 and 3.46 Hz, and the natural frequency of the roll mode is 3.96 Hz when the front and rear suspension stiffness is $10k_f$ and $10k_r$. Considering these natural frequencies, the oscillation of 3.42 Hz in the bounce displacement is due to the bounce-pitch mode with 3.46 Hz, while the oscillation with 4.00 Hz in roll angle is due to the roll mode with 3.96 Hz.

The oscillation amplitudes of the bounce acceleration shown in Figure 21a, and the roll angular acceleration shown in Figure 21b increase with the suspension stiffness. The oscillation frequencies for these accelerations are the same as those for the displacements in Figure 20, and as mentioned above, these oscillations occur owing to the natural vibrations of the bounce-pitch and roll modes. The increase in the acceleration values of the bounce and roll may adversely affect the riding comfort and steering stability that passengers can feel.

Preprints (www.preprints.org) | NOT PEER-REVIEWED | Posted: 19 April 2023 doi:10.20944/preprints202304.0529.v1

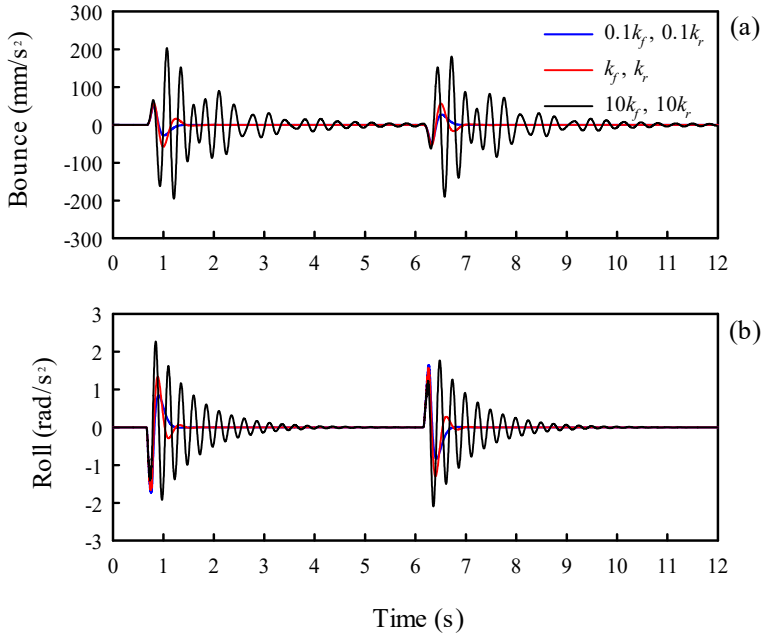

Figure 21. Dynamic responses of the accelerations for three values of the suspension stiffness: (a) the bounce and (b) the roll.

Next, we analyze the effects of suspension damping on the dynamic responses for the bounce and roll motions of the sprung mass. Based on the damping values c_f and c_r of the front and rear suspensions presented in Section 2, the dynamic responses of the vehicle were calculated for three damping values of 0.5, 1, and 1.5 times these values. Damping values of 0.1, 1, and 10 times c_f and c_r were not used because the vehicle system with $10c_f$ and $10c_r$ showed unrealistic overdamped motion. Figure 22, which shows displacements for three damping values of 0.1, 1, and 10 times c_f and c_r, demonstrates that the oscillation amplitudes of the bounce displacement and roll angle decrease as damping increases. This phenomenon is also observed in Figure 23, which shows the bounce acceleration and roll angular acceleration. As is well known, suspension damping contributes to reducing the dynamic responses of the vehicle; therefore, it improves the ride comfort and cornering feeling of the vehicle.

Finally, the effects of the torsional stiffness of the anti-roll bar on the dynamic responses for the bounce and roll motions are considered. Based on the torsional stiffness κ_f and κ_r of the front and rear anti-roll bars presented in Section 2, simulations for the step steer test were performed for the three torsional stiffness values of 0.1, 1, and 10 times κ_f and κ_r. The dynamic responses of the bounce displacements and roll angles for these three torsional stiffness values are shown in Figure 24. This figure illustrates that the larger the torsional stiffness, the smaller not only the bounce displacement and roll angle, but also their oscillation amplitudes. Figure 25 also shows that the amplitudes of the bounce acceleration and roll angular acceleration decrease as the torsional stiffness increases. Consequently, as shown in Figures 24 and 25, the increase in the torsional stiffness of the anti-roll bar provides a more comfortable driving environment to the driver by reducing the roll and bounce motions.

Preprints (www.preprints.org) | NOT PEER-REVIEWED | Posted: 19 April 2023 doi:10.20944/preprints202304.0529.v1

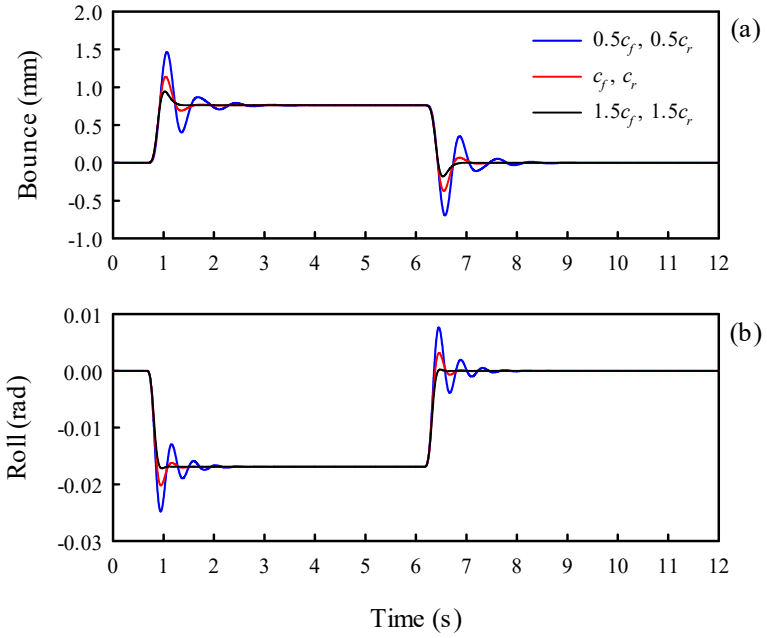

Figure 22. Dynamic responses of the displacements for three values of the suspension damping: (a) the bounce and (b) the roll.

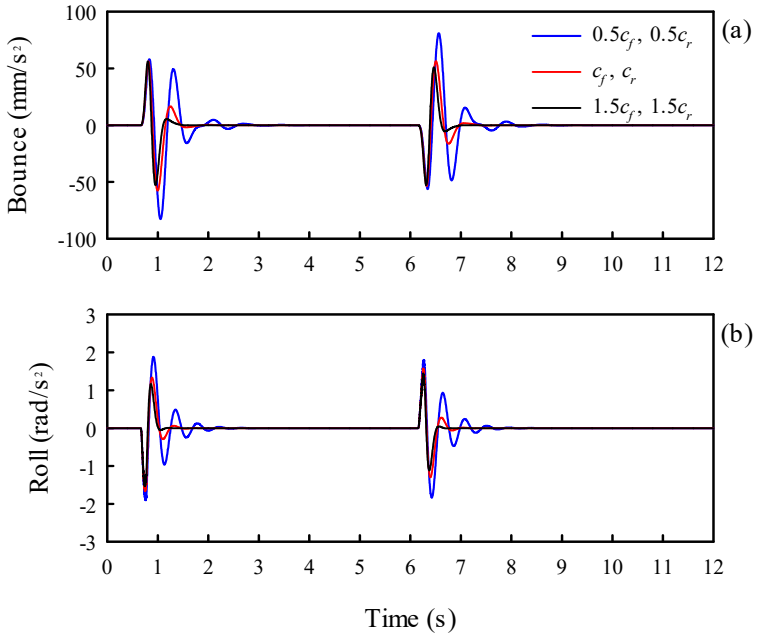

Figure 23. Dynamic responses of the accelerations for three values of the suspension damping: (a) the bounce and (b) the roll.

Preprints (www.preprints.org) | NOT PEER-REVIEWED | Posted: 19 April 2023 doi:10.20944/preprints202304.0529.v1

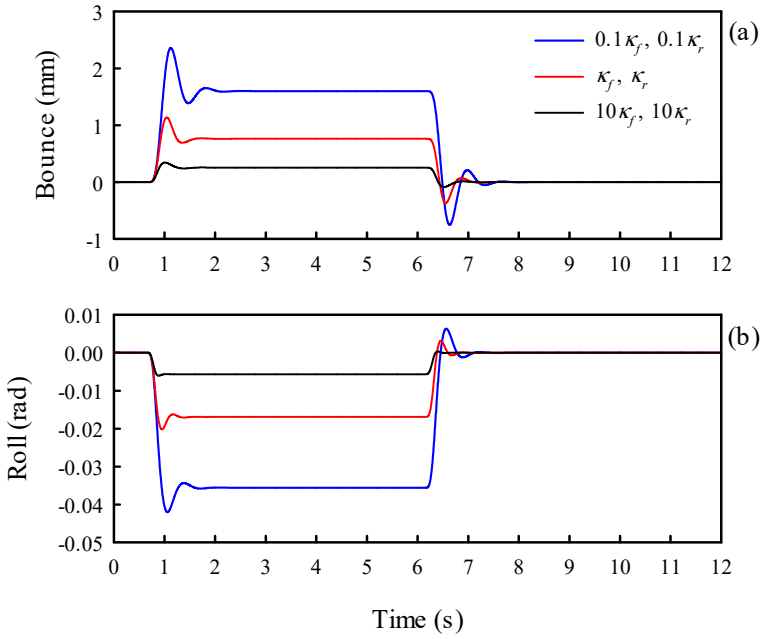

Figure 24. Dynamic responses of the displacements for three values of the torsional stiffness of the anti-roll bar: (a) the bounce and (b) the roll.

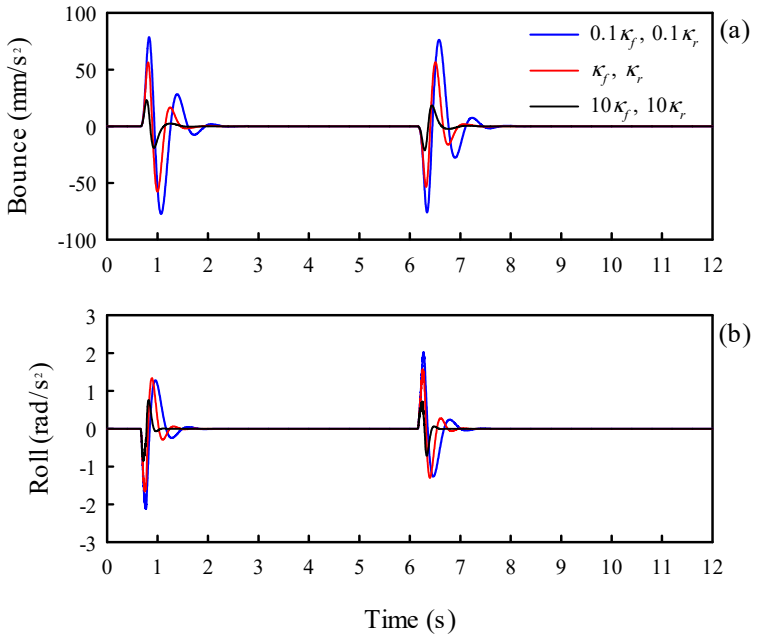

Figure 25. Dynamic responses of the accelerations for three values of the torsional stiffness of the anti-roll bar: (a) the bounce and (b) the roll.

5. Conclusions

This study presents a dynamic vehicle model that can analyze the dynamic behavior of a vehicle without an actual driving test. Considering the centrifugal force acting on the vehicle during turning and the torsional stiffness of the anti-roll bar, a vehicle model with seven degrees of freedom was constructed to investigate the dynamic characteristics and responses to driving conditions. The equations of motion for this vehicle model were derived using Lagrange's equation. The constructed vehicle model was verified by comparing the suspension deformations computed by the simulations with the deformation measured through actual driving tests. Using this model, the natural

frequencies and mode shapes of the vehicles were analyzed. Moreover, the effects of the suspension stiffness and anti-roll bar torsional stiffness on the natural frequencies were also analyzed. In addition, the effects of suspension stiffnesses, suspension damping coefficients, and anti-roll bar torsional stiffnesses on the dynamic responses of the vehicle were also investigated when the vehicle was under the step steer test. The results obtained in this study can be applied not only to internal combustion engine vehicles but also to electric and hybrid vehicles.

The results of analyzing the dynamic characteristics of the driving vehicle using the proposed dynamic model are summarized as follows:

- The natural frequencies of the vibration modes associated with the sprung mass were much lower than those of the modes associated with the unsprung masses.
- When one of the front and rear wheel suspension stiffnesses increases, the natural frequencies for the roll mode, the associated wheel modes, and one of the bounce-pitch modes increase, whereas the frequencies of the other modes remain constant.
- When both the front- and rear-wheel suspension stiffnesses increase simultaneously, the natural frequencies of all modes for the sprung and unsprung masses increase.
- When only one of the two anti-roll bars torsional stiffnesses increases, the natural frequencies of the roll mode and the corresponding out-of-phase wheel mode increase, while the natural frequencies of the other modes remain unchanged.
- When the two torsional stiffnesses of the front and rear anti-roll bars increase simultaneously, the natural frequencies of the roll mode and out-of-phase wheel modes increase, while those of the bounce-pitch modes and the in-phase wheel modes remain unchanged.

When performing the step steer test, the analysis results of the effects of design parameters such as suspension stiffness, suspension damping, and anti-roll bar torsional stiffness on the dynamic responses of the vehicle model are as follows.

- The bounce displacement and roll angle decrease with the suspension stiffness.
- When the suspension stiffness is large, the bounce displacement and roll angle have high-frequency oscillations because of the bounce-pitch mode and the roll mode.
- The oscillation amplitudes in the bounce acceleration and roll angular acceleration increase with the suspension stiffness.
- Suspension damping contributes to reducing the dynamic responses of the vehicle, including both the displacements and accelerations for bounce and roll motions.
- The torsional stiffness of the anti-roll bar reduced both the displacements and accelerations of the bounce and roll motions.

Author Contributions: Conceptualization, J.C. and M.C.; methodology, J.C. and S.Y.; software, S.Y., J.L. and D.K.; validation, W.J. and M.C.; formal analysis, S.Y., and J.L.; investigation, S.Y., J.L., W.J. and D.K.; resources, D.K. and M.C.; data curation, S.Y. and W.J.; writing—original draft preparation, S.Y.; writing—review and editing, M.C. and J.C.; visualization, S.Y.; supervision, J.C.; project administration, J.C.; funding acquisition, J.C. All authors have read and agreed to the published version of the manuscript.

Funding: This work was partially funded by the National Research Foundation of Korea (NRF) through a grant from the Korean Government (MEST) (NRF-2021R1A2C2007979) and the Korea Institute for Advancement of Technology (KIAT) grant from the Korea Government (MOTIE) (P0012769, HRD Program for Industrial Innovation).

Institutional Review Board Statement: Not applicable.

Informed Consent Statement: Not applicable.

Data Availability Statement: Not applicable.

Conflicts of Interest: The authors declare no conflict of interest.

References

1. Choi, S.B.; Lee, H.K.; Chang, E.G. Field test results of a semi-active ER suspension system associated with skyhook controller. *Mechatronics.* **2001**, *11*, 345-353.
2. Jonsson, P.; Johansson, O. Prediction of vehicle discomfort from transient vibrations. *J. Sound Vib.* **2005**, *282*, 1043-1064.
3. Uys, P.E.; Els, P.S.; Thoresson, M.J. Criteria for handling measurement. *J. Terramech.* **2006**, *43*, 43-67.

4. Darling, J.; Hickson, L.R. An Experimental Study of a Prototype Active Anti-Roll Suspension System. *Veh. Syst. Dyn.* **1998**, 29, 309-329.
5. Choi, S.B.; Han, Y.M.; Song, H.J.; Sohn, J.W.; Choi, H.J. Field test on vibration control of vehicle suspension system featuring ER shock absorbers. *J. Intell. Mater. Syst. Struct.* **2007**, 18, 1169-1174.
6. Sun, T; Zhang, Y.; Barak, P. Quarter Vehicle Ride Model. *SAE Paper Series 2002-01-1581.* **2002**.
7. Georgiou, G.; Verros, G.; Natsiavas, S. Multi-objective optimization of quarter-car models with a passive or semi-active suspension system. *Veh. Syst. Dyn.* **2007**, 45, 77-92.
8. Singh, D.; Aggarwal, M.L. Passenger seat vibration control of a semi-active quarter car system with hybrid Fuzzy-PID approach. *Int. J. Dyn. Control.* **2015**, 5, 287-296.
9. Singh, D. Ride comfort analysis of passenger body biodynamics in active quarter car model using adaptive neuro-fuzzy inference system based super twisting sliding mode control. *J. Vib. Control.* **2019**, 25, 1866-1882.
10. Sun, T.; Zhang, Y.; Barak, P. 4-DOF Vehicle Ride Model. *SAE Paper Series 2002-01-1580.* **2002**.
11. Zhu, H.; Yang, J.; Zhang, Y. Modeling and optimization for pneumatically pitch-interconnected suspension of a vehicle. *J. Sound Vib.* **2018**, 432, 290-309.
12. Hudha, K.; Jamaludding, H.; Samin, P.M.; Rahman, R.A. Semi Active Roll Control Suspension (SARCS) System on a New Modified Half Car Model. *SAE Paper Series 2003-01-2274.* **2003**.
13. Gosselin-Brisson, S.; Bouazara, M.; Richard, M.J. Design of an active anti-roll bar for off-road vehicles. *Shock Vib.* **2019**, 16, 155-174.
14. Abu Barak, S.A.; Samin, P.M.; Azhar, A.A. Modelling and Validation of Vehicle Ride Comfort Model. *Appl. Mech. Mater.* **2014**, 554, 515-519.
15. Palli, S.; Sharma, R.C.; Rao, P.P.D. Dynamic Behaviour of a 7 DoF Passenger Car Model. *Int. J. Veh. Struct. Syst.* **2017,** 9, 57-63.
16. Senthilkumar, P.; Sivakumar, K.; Kanagarajan, R.; Kuberan, S. Fuzzy Control of Active Suspension System using Full Car Model. *Mechanika.* **2018**, 24, 240-247.
17. Ghike, C.; Shim, T. 14 Degree-of-Freedom Vehicle Model for Roll Dynamics Study. *SAE Paper Series 2006-01-1277.* **2006**.
18. Julio-Rodríguez, J.d.C.; Santana-Díaz, A.; Ramirez-Mendoza, R.A. Individual Drive-Wheel Energy Management for Rear-Traction Electric Vehicles with In-Wheel Motors. *Appl. Sci.* **2021**, 11, 4679.
19. Trzesniowski, M. In *Steering Kinematics*, Harrer, M., Pfeffer, P., Eds.; Cham: Switzerland, 2017; pp. 398-402.
20. Cong, S.; Shangbin, S.; Zan, L. Vehicle roll stability analysis considering lateral-load transfer rate. In Proceedings of the International Conference on Transportation Information and Safety (ICTIS) 2015, Wuhan, China, 25–28 June 2015; pp. 398–402.
21. Yoon, D.S.; Kim, G.W.; Choi, S.B. Response time of magnetorheological dampers to current inputs in a semi-active suspension system: Modeling, control and sensitivity analysis. *Mech. Syst. Signal Proc.* **2021**, 146, 106999.
22. Lajqi, S.; Gugler, J.; Lajqi, N.; Shala, A.; Likaj, R. Possible experimental method to determine the suspension parameters in a simplified model of a passenger car. *Int. J. Automot. Technol.* **2012**, 13, 615–621.
23. Taylor, R.; Bashford, L.; Schrock, M. Methods for measuring vertical tire stiffness. *Trans. ASAE.* **2000**, 43, 1415.
24. Newmark, N.M. A method of computation for structural dynamics. *J. Engrg. Mech. Div.* **1959**, 85, 67-94.
25. Sorniotti, A.; D'Alfio, N. Vehicle Dynamics Simulation to Develop an Active Roll Control System. In *SAE Technical Paper*, No. 2007-01-0828; SAE International: Warrendale, PA, USA, **2007**.
26. Zhang, J.; Wang, M. Integrated Adaptive Steering Stability Control for Ground Vehicle with Actuator Saturations. *Appl. Sci.-Basel.* **2022**, 12, 8502.
27. Chen, H.; Gong, M.-D.; Zhao, D.-X.; Liu, W.-B.; Jia, G.-Y. Coordination Control of Multi-Axis Steering and Active Suspension System for High-Mobility Emergency Rescue Vehicles. *Mathematics.* **2022**, 10, 3562.